

Determination of the Venus eddy diffusion profile from CO and CO₂ profiles using SOIR/Venus Express observations

A. Mahieux^{a,b,*}, R.V. Yelle^c, N. Yoshida^d, S. Robert^{a,e}, A. Piccialli^a, H. Nakagawa^d, Y. Kasaba^d, F.P. Mills^{b,f,g}, A.C. Vandaele^a

^a Royal Belgian Institute for Space Aeronomy, Brussels, Belgium

^b The University of Texas at Austin, Austin, TX, United States of America

^c The University of Arizona, Tucson, AZ, United States of America

^d Tohoku University, Sendai, Japan

^e Institute of Condensed Matter and Nanosciences, Université catholique de Louvain, Chemin du Cyclotron 2, 1348 Louvain-la-Neuve, Belgium

^f Space Science Institute, Boulder, Colorado, United States of America

^g The Australian National University, Canberra, ACT, Australia

ARTICLE INFO

Keywords:

Venus
Eddy diffusion coefficient
Modelling
Mesosphere
Thermosphere

ABSTRACT

We present a study of the SOIR/Venus Express CO₂ and CO profiles in order to constrain the eddy diffusion profile in the Venus mesosphere (80 to 130 km of altitude). We compute the mean number density profile of both species, and the hydrostatic temperature based on the CO₂ mean density profile. We use a 1D-photochemical/diffusion model to adjust the eddy diffusion profile such that the 1D-model and SOIR CO profiles best agree. We compare our results with eddy diffusion profiles found in the literature. We use our approach to revisit the He and CO₂ profiles from Pioneer Venus probe mass spectrometer in order to derive an eddy diffusion profile extending from 80 to 200 km of altitude. Our eddy diffusion profile is different in shape and in magnitude compared to the Pioneer Venus profile: it is equal to 3.6×10^6 cm²/s at 110 km, 7.5×10^6 cm²/s at 120 km, 0.4×10^6 cm²/s at 130 km, and 201×10^6 cm²/s at 140 km, and constant below 110 km and above 140 km. This new eddy diffusion profile can be used in Venus Global Circulation Models as well as 1D-photochemical models.

1. Introduction

The eddy diffusion coefficient, K_{zz} , is used to parameterize the efficiency of vertical transport in planetary atmospheres. K_{zz} characterizes in an approximate way vertical mixing of constituents due to motions that violate the Eliassen-Palm theorem (Edmon Jr et al., 1980), i.e. motions must be dissipative, non-linear, or unsteady in some manner. Since these motions can occur on a wide variety of macroscopic spatial scales, and that perturbations tend to grow exponentially with altitude, it is impossible to calculate K_{zz} in a planetary atmosphere and no reliable models exist. Instead, K_{zz} must be determined through comparison with observations. Despite its empirical and somewhat ad-hoc nature, an adequate value of K_{zz} at each pressure level is still essential in planetary atmospheres studies, especially for photochemical models. Although many Global Circulation Models (GCMs) include chemistry and transport by advection, the chemistry tends to be simplified and simulations can only be run for relatively short periods of times (~weeks), while in

many atmospheres, some chemical species take years to come to equilibrium. Moreover, it is often unclear if the advection simulated by GCMs includes the range of motions found in an actual atmosphere. This means there is still a place for 1D-photochemical models that can simulate chemical cycles over long periods of time and can include extremely complex chemistry. These 1D-photochemical models require an eddy diffusion profile to parametrize vertical transport.

Recent investigations by Zhang et al. (2012) and Parkinson et al. (2015a) employed 1D-photochemical models to study the distribution of sulfur species and H₂O, respectively, in the Venus middle atmosphere, up to 112 km. Both these studies emphasize the importance of vertical transport for the chemistry of these species but do not investigate K_{zz} in detail. In fact, to the best of our knowledge, the only observationally based estimate of K_{zz} of the Venus mesosphere and thermosphere comes from analysis of mass spectrometer data on the Pioneer Venus probe (von Zahn et al., 1980), which were available from 200 km down to 120 km of altitude. These authors used the vertical distribution of He and N₂,

* Corresponding author at: Royal Belgian Institute for Space Aeronomy, Brussels, Belgium.

E-mail address: arnaud.mahieux@aeronomie.be (A. Mahieux).

<https://doi.org/10.1016/j.icarus.2021.114388>

Received 23 September 2020; Received in revised form 29 January 2021; Accepted 15 February 2021

Available online 22 February 2021

0019-1035/© 2021 The Authors. Published by Elsevier Inc. This is an open access article under the CC BY license (<http://creativecommons.org/licenses/by/4.0/>).

both inert gases, to estimate K_{zz} near the homopause at 136 km for N_2 , and 130 km for He. The studies of mesospheric chemistry, however, require K_{zz} at lower altitude, from the cloud top to ~ 130 km. Estimates of K_{zz} at the cloud top were provided by Lane and Opstbaum (1983) using high vertical resolution scans of the Venus limb made by the Pioneer Venus Orbiter Cloud Photopolarimeter and by Woo et al. (1980) using Pioneer Venus radio occultation measurements.

The homopause, also named turbopause, is the altitude region where the eddy diffusion coefficient becomes larger than the molecular diffusion coefficient (Banks and Kockarts, 1973). It forms the separation region between the homosphere located below, where inert gases are well mixed, and transport is dominated by eddy diffusion, by opposition to the heterosphere where molecular diffusion takes over and molecular species separate according to their molecular weights. In the homosphere, all inert species vary with altitude with the same scale height, computed from the mean atmospheric molecular mass, while in the heterosphere each species follows its own scale height based on its own molecular mass.

The SOIR instrument on Venus Express measured the altitude profiles of a variety of species including CO_2 and CO (Vandaele et al., 2016a). Although not as inert as the He and N_2 utilized in the von Zahn et al. (1980) studies, CO is, nevertheless, fairly unreactive, particularly at higher altitudes. CO is produced primarily by CO_2 photodissociation and destroyed by a variety of chemical reactions, especially OH + CO (Yung and DeMore, 1982; Zhang et al., 2012), and via catalytic cycles involving ClCO and ClCO₃ (Krasnopolsky and Parshev, 1983; Yung and DeMore, 1982), primarily at altitudes below 85 km. Above ~ 90 km, the abundances of OH and ClCO are sufficiently small that production of CO_2 from CO is slow ($< 5\text{--}7\%$ of the modeled column total (Mills and Allen, 2007; Zhang et al., 2012)). Other losses for CO, e.g. ionization, should be even smaller (Fox and Bougher, 1991). At 85–90 km altitude, production of CO_2 from CO increases to $\sim 15\text{--}25\%$ of the modeled column total and becomes comparable to modeled CO flux divergence (Mills and Allen, 2007; Zhang et al., 2012). Thus, at altitudes above 85 km the CO distribution should be determined by production from photolysis and eddy diffusion downward. We utilize this to characterize K_{zz} in the middle atmosphere. By comparing models for the CO distribution based on photolytic production and diffusion with the averaged SOIR profiles, we constrain K_{zz} from 85 to 130 km. We show that at the lower end of this altitude range K_{zz} is much larger than assumed by von Zahn et al. (1980) or used in the models of Zhang et al. (2012) and Parkinson et al. (2015a).

The next section presents the SOIR instrument and its dataset and discusses how we construct the averaged CO, CO_2 , and temperature profiles. Our photochemical/diffusion model is discussed in section 3, where we also discuss the eddy diffusion profile. Finally, we give our conclusions in section 4.

2. The SOIR database

2.1. The SOIR instrument

SOIR (Solar Occultation in the InfraRed) was a fast, powerful and compact instrument on board the ESA Venus Express (VEx) spacecraft (Nevejans et al., 2006). Using an echelle grating as the diffracting element and an Acousto-Optical Tunable Filter (AOTF) for order sorting, SOIR had the ability to record simultaneously four different narrow regions ($\sim 24\text{ cm}^{-1}$ wide) in the 2200–4400 cm^{-1} wavenumber region (Mahieux et al., 2008). SOIR resolved the ro-vibrational absorption lines of many species absorbing in that wavelength range, such as CO_2 (Mahieux et al., 2015a), CO (Vandaele et al., 2016b), HCl and HF (Mahieux et al., 2015c), H_2O (Chamberlain et al., 2020) and SO_2 (Mahieux et al., 2015b), which could all be measured simultaneously. Its viewing geometry was solar occultation and observations span up to 100 km altitude range. SOIR could detect CO_2 up to altitudes of 170 km and CO up to 140 km. The minimum altitude that could be measured

varied between 65 and 70 km, as, at lower altitudes, IR sunlight was completely absorbed by the Venus clouds and haze. The observations covered all latitudes on both sides of the terminator, except for the 60 to 65° North region, due to the highly elliptical shape of the VEX orbit.

Because SOIR was sensitive to carbon dioxide, the major constituent of the Venusian atmosphere, temperature profiles could be calculated assuming a hydrostatic equilibrium atmosphere (Mahieux et al., 2015a). Finally, considering the CO_2 volume mixing ratio from the Venus International Reference Atmosphere (Hedin et al., 1983; Zasova et al., 2006), computed the total pressure could be computed (Mahieux et al., 2015a).

Since K_{zz} is a quantity relative to a mean atmosphere state, we consider mean profiles calculated from observations covering the full VEx mission, from May 2006 to November 2014. Furthermore, averaging the profiles also removes the effects of transient phenomena such as gravity waves present in the individual profiles.

The SOIR database contains 747 occultations; amongst them 279 occultations targeted simultaneously CO and CO_2 . In this work, we consider 208 observations of CO and CO_2 (75% of the available database). Some observations were indeed not considered because they were showing either too low signal to noise ratio, or the fit of either CO_2 or CO was not satisfactory. The location of the selected orbits as a function of latitude/longitude is given in Fig. 1A, and as a function of the orbit number/Earth year and latitude in Fig. 1B.

We note that some of the CO profiles were discussed in Vandaele et al. (2015) and Vandaele et al. (2016b), and the CO_2 and temperature profiles in Mahieux et al. (2012) and Mahieux et al. (2015a). The retrieval procedure is therefore not explained here. The individual CO_2 and CO profiles are available in the VESPA online database (Trompette et al., 2017).¹

2.2. Mean profiles calculation

To average the profiles, we consider a common pressure scale p to compute the weighted mean $n_{CO_2}(p)$, $n_{CO}(p)$ and $T(p)$ profiles, where the weights are the inverse of the uncertainties on the number densities or temperature values. We average on a pressure grid rather than altitude grid because atmospheric processes, including diffusion, depend closely on pressure whereas altitudes can be influenced by temperature variations at low altitudes, outside the range under investigation. Moreover, using a pressure instead of the altitude removes the effects of the large variability observed in the SOIR profiles (Mahieux et al., 2015a). We compute a mean altitude scale $z(p)$ using the hydrostatic equation and the CO_2 mean vertical density profile

$$z(p) = z_0 + \frac{1}{m_{CO_2} \cdot g} \int_p^{p_0} \frac{dp}{n_{CO_2}(p)} \quad (1)$$

where m_{CO_2} is the average mass of a CO_2 molecule (7.307×10^{-23} g) and g is the Venus gravity (882 cm/s^2). z_0 is taken as the mean altitude of the profiles at a pressure of 15.85 mbar, which corresponds to the highest pressure level at which there are at least 20 observations.

The mean temperature profile is not necessarily in hydrostatic equilibrium with the mean CO_2 profile, because the derivation of the temperature using the hydrostatic equilibrium equation is non-linear. For this reason, we compute a hydrostatic temperature profile $T_{hydro}(p)$ from the mean CO_2 profile. We use the following relation, assuming an isothermal temperature profile for the upper boundary condition

¹ http://vespa.obspm.fr/planetary/data/display/?&resource_id=ivo://bira-iasb/tap&resource_type=epn

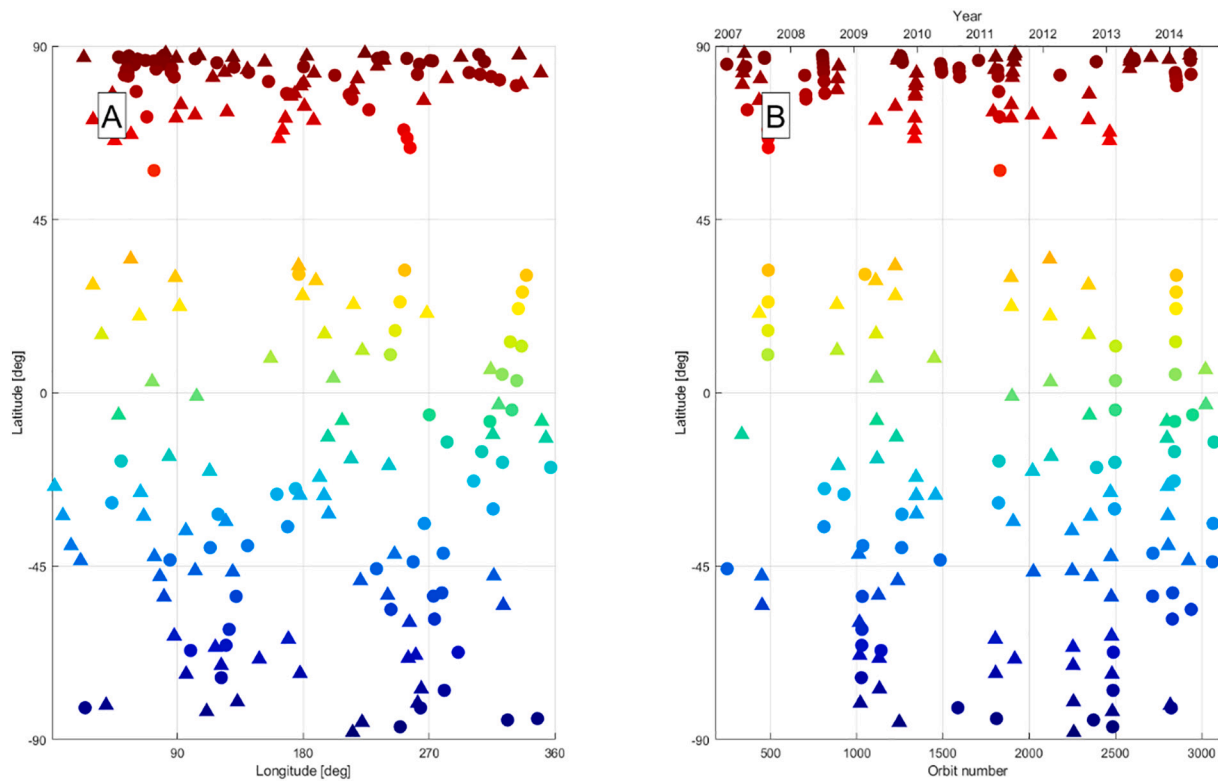


Fig. 1. Panel A: Longitude-latitude location of the observations considered in this work. Panel B: Orbit number/Earth year as a function of the latitude of the observations. The colour code is the latitude; the disks correspond to morning occultations, the triangles to evening. (For interpretation of the references to colour in this figure legend, the reader is referred to the web version of this article.)

$$T_{hydro}(z) = -\frac{m_{CO_2} \cdot g \int_z^{z_{max}} n(z') \cdot dz' + C}{k_B n(z)}$$

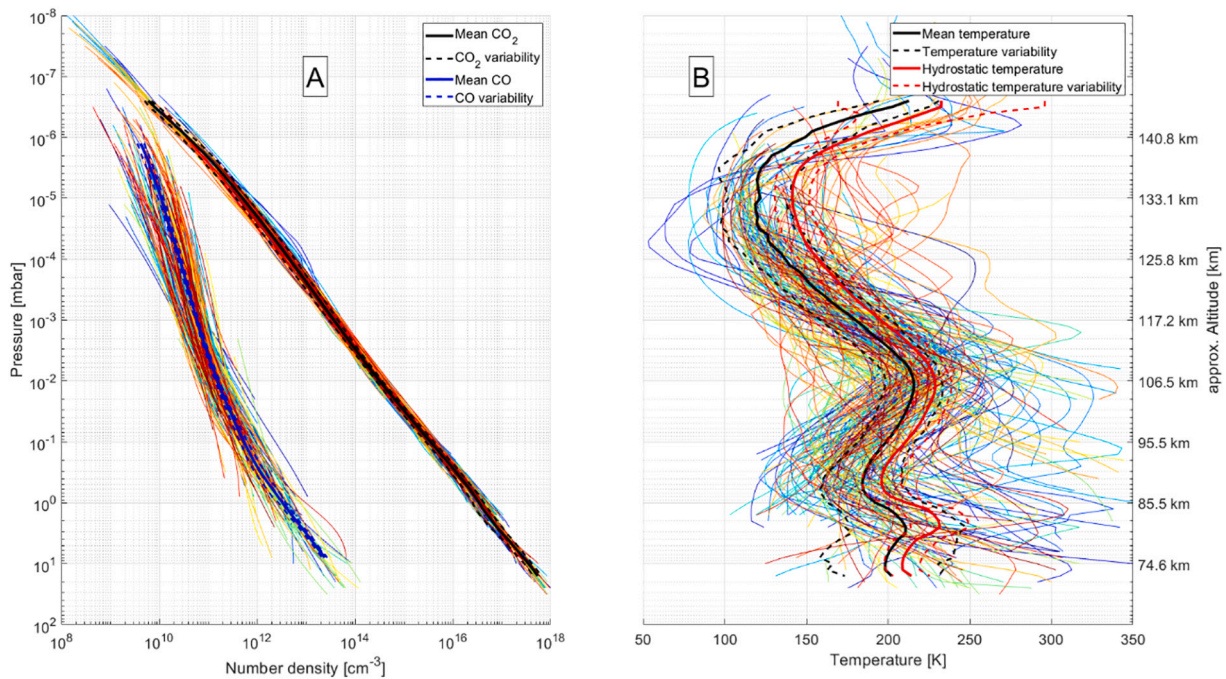


Fig. 2. CO and CO₂ number densities (Panel A) and temperature (Panel B) on a pressure scale, approximate altitudes are given on the right-hand side of Panel B. The colour code is the latitude, with the same colour code as in Fig. 1. The thick lines are the weighted mean profiles (Panel A: blue for CO, black for CO₂; Panel B: black for the mean temperature and red for the hydrostatic temperature), while the dashed profiles represent the variability (1-σ standard deviation). (For interpretation of the references to colour in this figure legend, the reader is referred to the web version of this article.)

$$C = \left(-\frac{n(z)}{d \log n(z)} \right) \Big|_{z_{\max}} \quad (2)$$

where k_B is the Boltzmann constant and z_{\max} is the uppermost altitude.

$n_{CO_2}(p)$ and $n_{CO}(p)$ are plotted in Fig. 2A and $T_{\text{mean}}(p)$ and $T_{\text{hydro}}(p)$ in Fig. 2B. There is a few Kelvins difference between the mean temperature profile and the hydrostatic temperature profile. We only consider the hydrostatic temperature profile T_{hydro} in the following, simply called temperature profile, noted T .

The expression of the hydrostatic partial pressure for species α is given by

$$p_\alpha(z) = p_\alpha(z_0) \cdot \exp\left(-\frac{m_\alpha \cdot g}{k_B} \int_{z_0}^z \frac{dz'}{T(z')}\right) \quad (3)$$

where $p_\alpha(z)$ is the partial pressure of species α and z_0 is some reference altitude. This expression may also be rewritten as

$$\log\left(\frac{n_\alpha(z) \cdot T(z_0)}{n_\alpha(z_0) \cdot T(z)}\right) = m_\alpha \cdot \left(-\frac{g}{k_B} \int_{z_0}^z \frac{dz'}{T(z')}\right) \quad (4)$$

If we take the ratio of expression (4) for CO and CO₂, assuming the perfect gas law, we derive the following expression

$$\log\left(\frac{n_{CO}(z) \cdot T(z_0)}{n_{CO}(z_0) \cdot T(z)}\right) = \frac{m_{CO}}{m_{CO_2}} \cdot \log\left(\frac{n_{CO_2}(z) \cdot T(z_0)}{n_{CO_2}(z_0) \cdot T(z)}\right) \quad (5)$$

In Fig. 3, we use Eq. (5) with the SOIR mean CO₂, CO and temperature profiles. We plotted $\log\left(\frac{n_{CO}(z) \cdot T(z_0)}{n_{CO}(z_0) \cdot T(z)}\right)$ as a function of

$\log\left(\frac{n_{CO_2}(z) \cdot T(z_0)}{n_{CO_2}(z_0) \cdot T(z)}\right)$. The black curve is the data. The series of red lines have a slope of $\frac{m_{CO}}{m_{CO_2}}$, i.e. CO and CO₂ have their own scale heights, while the series of blue lines have a slope of 1, i.e. CO and CO₂ have the same scale height. Between 76.7 km and ~90 km, the slope of the data is nearly equal to 1, as expected in the homosphere since both species have the same scale height. Above 135 km, the slope is getting closer to $\frac{m_{CO}}{m_{CO_2}}$, which should be the case in the heterosphere. In between these altitudes, the slope varies and is even larger than $\frac{m_{CO}}{m_{CO_2}}$ between ~105 and ~130 km. This indicates that another atmospheric process occurs in that

altitude region, that we attribute to CO produced by CO₂ photodissociation (Inn and Heimerl, 1971; Ityakov et al., 2008). CO₂ photodissociation by solar UV occurs at wavelength lower than 200 nm and produces CO and O atoms (Krasnopolsky, 2012; Yung and DeMore, 1982). The existence of this photochemical process motivates the use of a 1D-photochemical/diffusion model to determine the altitude of the homopause and constrain the eddy diffusion profile $K_{zz}(z)$.

3. Determination of the eddy diffusion profile using a 1D-photochemical/diffusion model

3.1. Model description

We consider a 1D-photochemical/diffusion model assuming a plane-parallel atmosphere under hydrostatic conditions (Yelle et al., 2014), and where the composition is made of two species, CO₂ and CO. We solve at each time step the time dependent continuity equation

$$\frac{\partial n_i(z, t)}{\partial t} = P_i(z, t) - \frac{\partial \Phi_i(z, t)}{\partial z} \quad (6)$$

where $n_i(z, t)$ is the number density profile of species i , $P_i(z, t)$ is the production rate, $\Phi_i(z, t)$ is the diffusive vertical flux. The flux is computed using the minor species diffusion approximation

$$\Phi_i(z, t) = -D_i(z) \cdot \left(\frac{\partial n_i(z, t)}{\partial z} + n_i(z, t) \cdot \left(\frac{1}{H_i(z)} + \frac{(1 + \alpha_i)}{T(z)} \frac{\partial T(z)}{\partial z} \right) \right) - K_{zz}(z) \cdot \left(\frac{\partial n_i(z, t)}{\partial z} + n_i(z, t) \cdot \left(\frac{1}{H_a(z)} + \frac{1}{T(z)} \frac{\partial T(z)}{\partial z} \right) \right) \quad (7)$$

where $D_i(z)$ is the average molecular diffusion coefficient, $H_i(z)$ is the density scale height of diffusing species i , $H_a(z)$ is the whole atmosphere scale height, $K_{zz}(z)$ is the eddy diffusion coefficient, and α_i is the thermal diffusion. In the following, all α_i are assumed equal to zero, as they all have infinitesimal values. The average molecular diffusion coefficients are calculated using the relation

$$D_i(z) = \frac{1}{k_B} \cdot \left(\sum_{j \neq i} n_j(z) \right)^{-1} \quad (8)$$

where b_{ij} are the binary diffusion parameters between species i and j

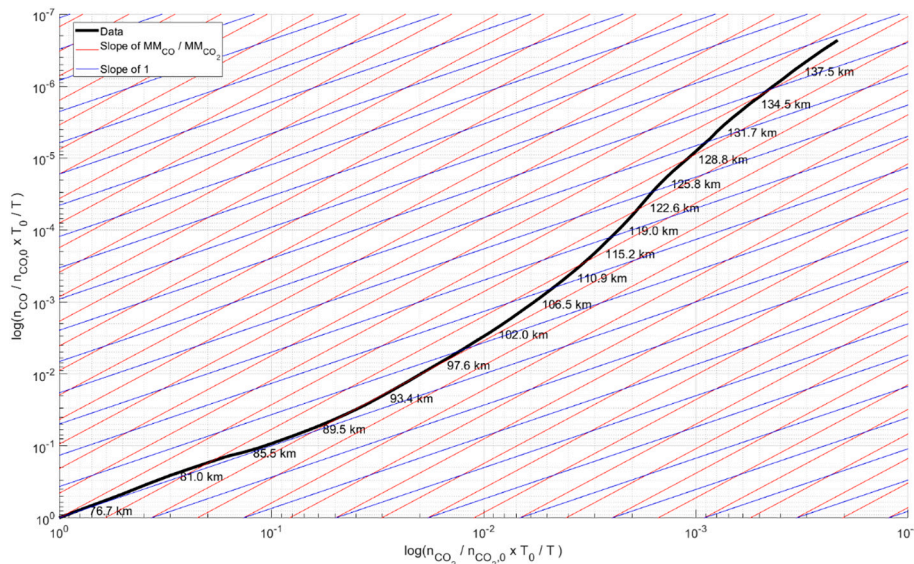


Fig. 3. Application of Eq. (5) to the SOIR mean profiles of CO₂, CO, and temperature. The blue curves show the slopes equal to 1; the red curves are the slopes equal to the ratio of the molar masses. The altitudes are also indicated. Note that the direction of both axes is reversed. (For interpretation of the references to colour in this figure legend, the reader is referred to the web version of this article.)

whose temperature dependence is given by $A_{ij} \cdot T^{s_{ij}-1}$ (Marrero and Mason, 1972). The coefficients A_{ij} and s_{ij} are taken from Table 13 of Marrero and Mason (1972). The velocity of each species is set to zero at the upper boundary, as thermal escape is negligible. At the lower boundary, the number density of each species is kept constant. We hold the temperature profile unchanged in the simulation, since we do not include any radiative term.

We include four photodissociation reactions



We set up a photodissociation cutoff at 200 nm. As explained in section 1, we do not consider reactions destroying CO. For this reason, we set up our lower boundary at 85 km. Instead, CO is transported downwards and, presumably, destroyed by reactions below the lower boundary of our simulations, as described in the introduction section. We do not keep track of the oxygen atom and ion products in the simulations.

The solar spectrum (Woods et al., 2005), CO₂ and CO absorption cross sections at a temperature of 295 and 298 K, respectively (Chan et al., 1993; Huestis and Berkowitz, 2010), and yield coefficients (Chan et al., 1993; Lawrence, 1972; Okabe, 1978) are plotted in Fig. 4. The sum of the yield coefficients is not equal to 1 at wavelengths lower than 200 nm, as the corresponding yield coefficients are related to CO₂ ionization reactions are not considered in this work. We also consider the CO₂ cross section at 195 K (Parkinson et al., 2003; Stark et al., 2007; Yoshino et al., 1996), and interpolate the cross sections for temperatures between 195 and 295 K.

The CO₂ photodissociation rate is computed using the following relation

$$P_{\text{CO}_2}(z) = d_{\text{av}} \cdot \int \exp\left(-\frac{\tau(z, \lambda)}{\mu}\right) \cdot \left(S_{\lambda}(\lambda) \cdot \frac{\lambda}{h \cdot c}\right) \cdot \epsilon_{UV}(\lambda) \cdot \sigma_{\text{CO}_2}(\lambda) \cdot n_{\text{CO}_2}(z) \cdot d\lambda \quad (9)$$

where $d_{\text{av}} = \frac{1}{2}$ is accounting for the diurnal averaging, μ is the cosine of the zenith angle, taken as 60°, $\tau(z, \lambda)$ is the optical depth at altitude z calculated from the CO₂ and CO absorption cross sections and number

density profiles, $S_{\lambda}(\lambda)$ is the solar irradiance, h is the Planck constant, c is the speed of light, and $\epsilon_{UV}(\lambda)$ is the sum of the yield coefficients.

Other species are present in the studied altitude range, such as N₂, He, O and various ions. We do not include them in the simulation for the sake of simplicity, as they would not significantly affect the local optical depth in Eq. (9).

We discretize Eqs. (6) to (9) on a vertical grid with 1 km altitude steps. During a model simulation, we run the 1D-photochemical/diffusion model until steady state is reached, such that the maximum variation of the CO number densities with time become negligible: $\max\left(\left|\frac{dn_i}{dt}\right|\right) < 10^{-5} \text{ cm}^{-3}/\text{s}$. Steady state usually occurs after 200 to 1000 steps with a time step of 10⁴ s. Since the mean CO₂ profile is in hydrostatic equilibrium with the temperature profile, the CO₂ number density variations with time are close to zero.

In the following section, the model is used to minimize the difference between the data mean profile and the model steady state profile. We use the MATLAB Levenberg-Marquardt algorithm for fitting the model to the data.

3.2. Application to the SOIR mean profiles

3.2.1. SOIR mean profiles

The mean vertical profiles calculated from the SOIR database that are used in the following, are given in Fig. 5. The number density and temperature vertical profiles are the same mean profiles as the ones displayed in Fig. 2.

The fixed values of the number densities at the lower boundary (85 km) are equal to $3.37 \times 10^{16} \text{ cm}^{-3}$ for CO₂ and $3.24 \times 10^{12} \text{ cm}^{-3}$ for CO, which are equal to the mean SOIR CO₂ and CO number densities at those altitudes. Fixing the number density values at the lower boundary of the domain induces non-zero vertical fluxes at those altitudes.

The column CO production rate is equal to $3.8 \times 10^{12} \text{ cm}^2/\text{s}$, which is of the same order of magnitude as reported by Yung and DeMore (1982), which are varying between 7.6 and $8.5 \times 10^{12} \text{ cm}^2/\text{s}$.

In the following sections, we will fit the 1D-model CO number density vertical profile to the SOIR mean CO profile by adjusting K_{zz} profiles. The reader will find a summary of our modelling results in Table 1.

3.2.2. Constant K_{zz} profile

First, we assume the most simple eddy diffusion profile: an altitude constant profile $K_{zz, \text{SOIR}, \text{Cst}}$ to best fit the 1D-model CO with mean SOIR CO number density profile. The steady state CO number density vertical

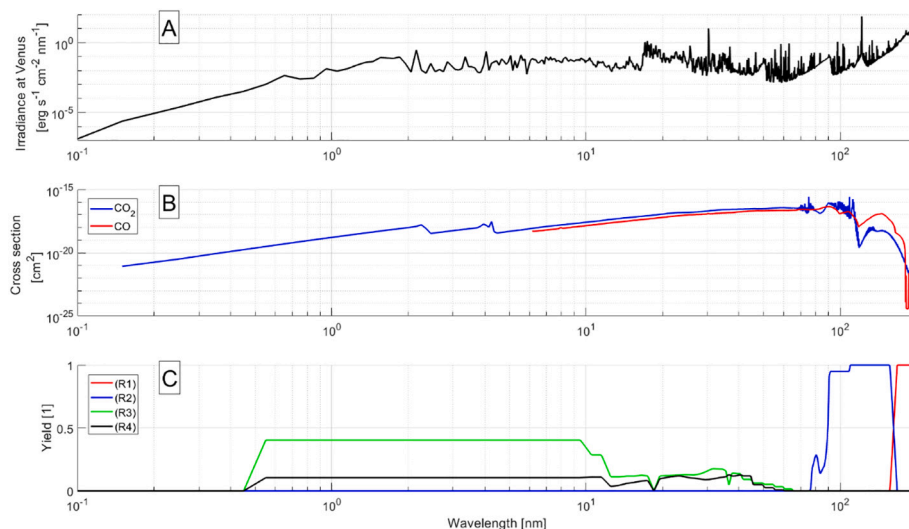


Fig. 4. Panel A: Solar irradiance corrected for Venus-Sun distance (Woods et al., 2005). Panel B: CO₂ (Huestis and Berkowitz, 2010) and CO absorption cross sections (Chan et al., 1993). Panel C: Yield coefficients (Chan et al., 1993; Lawrence, 1972; Okabe, 1978).

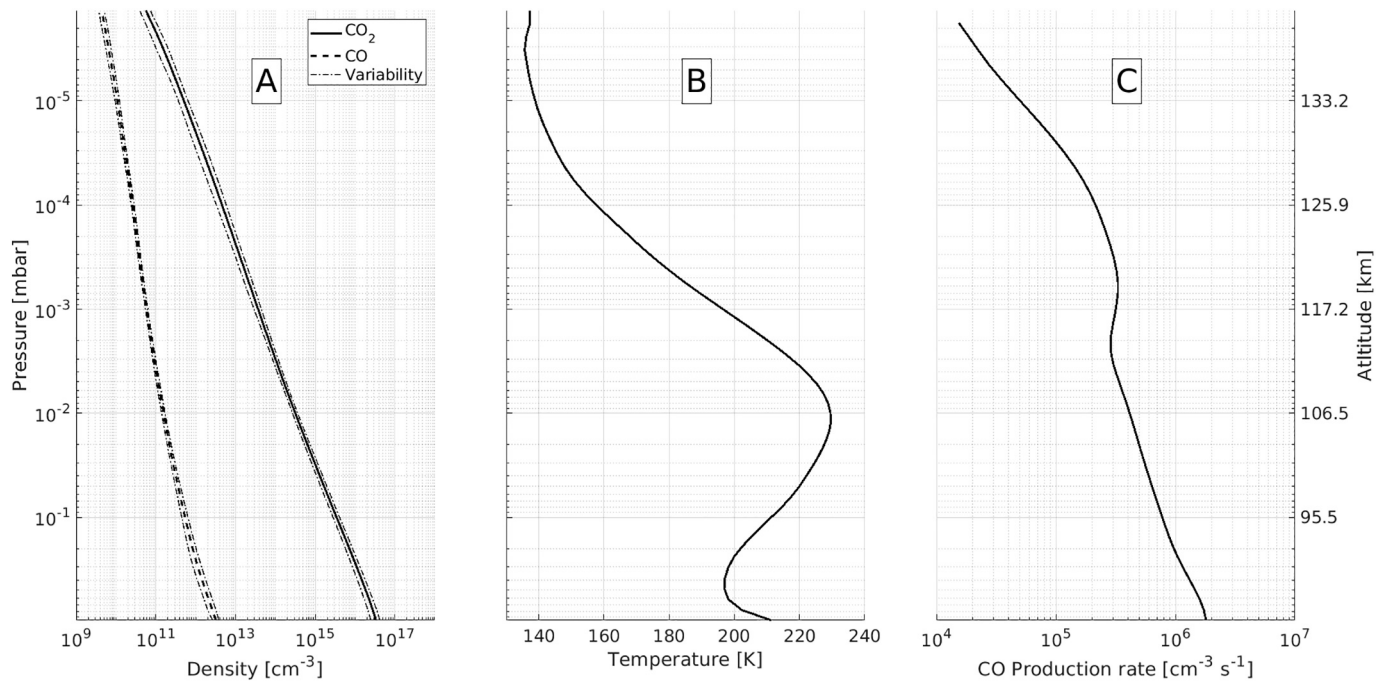


Fig. 5. The pressure scale is given on the left of Panel A and the altitude on the right of Panel C. Panel A: Number densities vertical profiles of CO₂ (solid) and CO (dashed) together with their variabilities (dash-dotted). Panel B: Mean temperature vertical profile. Panel C: CO production rate vertical profile resulting from the CO₂ photodissociation.

Table 1

Values of the eddy diffusion coefficients with altitude for the two cases considered in this work, with uncertainties obtained from the fits. The last two columns are values from the literature.

Altitude [km]	Constant eddy diffusion from SOIR dataset $K_{zz,SOIR, cst} [cm^2/s]$	Variable eddy diffusion from SOIR dataset $K_{zz,SOIR, var} [cm^2/s]$	Constant diffusion from PV and SOIR datasets $K_{zz, cst} [cm^2/s]$	Variable eddy diffusion from PV and SOIR dataset $K_{zz, var} [cm^2/s]$	Pioneer Venus eddy diffusion (von Zahn et al., 1980) $K_{zz, vZ} [cm^2/s]$	JPL eddy diffusion (Parkinson et al., 2015b) $[cm^2/s]$
80	$3.62 \times 10^6 \pm 8.4 \times 10^4$	$3.58 \times 10^6 \pm 4.2 \times 10^4$	$7.75 \times 10^6 \pm 2.3 \times 10^6$	$3.57 \times 10^6 \pm 2.3 \times 10^5$	$\sim 1 \times 10^5$	4×10^5
110	$3.62 \times 10^6 \pm 8.4 \times 10^4$	$3.58 \times 10^6 \pm 4.2 \times 10^4$	$7.75 \times 10^6 \pm 2.3 \times 10^6$	$3.57 \times 10^6 \pm 1.7 \times 10^5$	$\sim 8.7 \times 10^5$	2.6×10^6
120	$3.62 \times 10^6 \pm 8.4 \times 10^4$	$7.1 \times 10^6 \pm 1.2 \times 10^5$	$7.75 \times 10^6 \pm 2.3 \times 10^6$	$7.49 \times 10^6 \pm 5 \times 10^5$	$\sim 3.8 \times 10^6$	5×10^6
130	$3.62 \times 10^6 \pm 8.4 \times 10^4$	$4.98 \times 10^5 \pm 6.7 \times 10^3$	$7.75 \times 10^6 \pm 2.3 \times 10^6$	$3.98 \times 10^5 \pm 2.2 \times 10^4$	$\sim 1.7 \times 10^7$	9.3×10^6
140	$3.62 \times 10^6 \pm 8.4 \times 10^4$	$4.98 \times 10^5 \pm 6.7 \times 10^3$	$7.75 \times 10^6 \pm 2.3 \times 10^6$	$2.01 \times 10^8 \pm 2.1 \times 10^6$	$\sim 7.5 \times 10^7$	1.8×10^7
200	$3.62 \times 10^6 \pm 8.4 \times 10^4$	$4.98 \times 10^5 \pm 6.7 \times 10^3$	$7.75 \times 10^6 \pm 2.3 \times 10^6$	$2.01 \times 10^8 \pm 2.1 \times 10^6$	$\sim 5.4 \times 10^8$	1.8×10^7
RMS	0.256	0.115	0.433	0.162	–	–

profile are presented in Fig. 6A.

The CO number density root mean square (RMS), defined as

$$\sqrt{\frac{1}{N-1} \sum_{i=1}^N \left(\frac{n_{CO, model, cst}(z_i) - n_{CO, SOIR}(z_i)}{n_{CO, SOIR}(z_i)} \right)^2},$$

is equal to 0.256. The agreement between $n_{CO, model, cst}$ and $n_{CO, SOIR}$ is very good from 85 km up to 125 km. Above 130 km, $n_{CO, model, cst}$ is smaller than $n_{CO, SOIR}$ up to a factor 8. The best fit $K_{zz, SOIR, cst}$ is equal to $3.62 \times 10^6 \pm 8 \times 10^4$ cm²/s, see Fig. 6B.

3.2.3. Variable K_{zz} profile

Second, we consider an altitude variable eddy diffusion profile, $K_{zz, SOIR, var}$. $K_{zz, SOIR, var}$ is varied at three altitudes levels, every 10 km between 110 and 130 km, interpolated between those altitudes, and constant below 110 km and above 130 km. The profile is kept constant below 110 km since the previous fit with $K_{zz, SOIR, cst}$ showed that using a constant K_{zz} profile reproduces well the SOIR mean CO profile at those altitudes. The three fitting points were chosen to minimize the number of free parameters in the Levenberg-Marquardt fitting procedure while

maintaining good CO density fitting results.

The agreement between $n_{CO, model, var}$ and $n_{CO, SOIR}$ above 130 km is much better than in the previous case: $n_{CO, model, var}$ is given as the black plain profile in Fig. 6A. The CO number density RMS is equal to 0.115, much better than for a constant K_{zz} profile. This is due primarily to the decline in the parameter K_{zz} above 120 km. This result is reminiscent of the K_{zz} profile used in the terrestrial atmosphere (see for example Fig. 2 of Segura et al. (2007)). The decrease in K_{zz} could be due to a decrease in wave activity due to breaking of waves at lower altitudes and the damping of atmospheric motions by kinetic effects (viscosity, thermal conduction, molecular diffusion) at the low densities in the upper atmosphere.

The eddy diffusion profiles described above, $K_{zz, SOIR, var}$, shows values larger by several orders of magnitude than the one proposed by von Zahn et al. (1980), $K_{zz, vZ} = 1.4 \times 10^{13} \cdot n_a^{-\frac{1}{2}}$, with n_a the atmosphere total number density (see Table 1). $K_{zz, vZ}$ is plotted as the dotted profile in Fig. 6B. The steady state CO profile $n_{CO, model, vZ}$ computed using the von

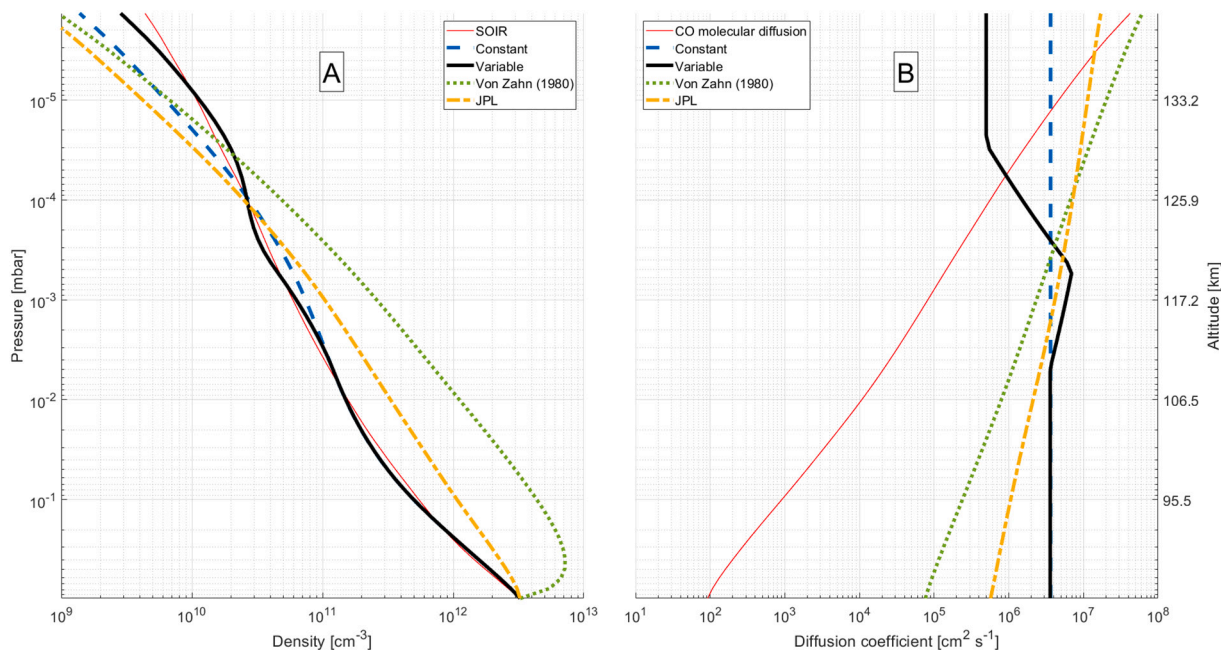


Fig. 6. The pressure scale is given on the left of Panel A and the altitude on the right of Panel B. Panel A: CO number density vertical profiles from SOIR ($n_{\text{CO, SOIR}}$, thin red solid, noted *SOIR*; it is the same as the black dashed line in Fig. 5A) computed with $K_{\text{zzSOIR, cst}}$ ($n_{\text{CO, modelcst}}$, blue dashed, noted *Constant*); computed with $K_{\text{zzSOIR, var}}$ ($n_{\text{CO, modelvar}}$, black solid, noted *Variable*); computed with K_{zzvZ} ($n_{\text{CO, modelvZ}}$, green dotted, noted *Von Zahn (1980)*); computed with K_{zzJPL} ($n_{\text{CO, modelJPL}}$, orange dash-dotted, noted *JPL*). Panel B: CO molecular diffusion coefficient (red thin solid); constant eddy diffusion coefficient $K_{\text{zzSOIR, cst}}$ (blue dashed, noted *Constant*); variable eddy diffusion coefficient $K_{\text{zzSOIR, var}}$ (black solid, noted *Variable*); *von Zahn et al. (1980)* eddy diffusion coefficient K_{zzvZ} (green dotted, noted *Von Zahn (1980)*); *Parkinson et al. (2015b)* eddy diffusion coefficient K_{zzJPL} (orange dash-dotted, noted *JPL*). (For interpretation of the references to colour in this figure legend, the reader is referred to the web version of this article.)

Zahn et al. (1980) diffusion coefficient is the dotted profile in Fig. 6A, and is overestimating $n_{\text{CO, SOIR}}$ up to 130 km by one order of magnitude, and underestimating them above that altitude.

We also considered the eddy diffusion coefficient used in the JPL/Caltech 1-D photochemistry model (*Parkinson et al., 2015b; Zhang et al., 2012*), K_{zzJPL} , depicted as the dash-dotted orange profile in Fig. 6B. K_{zzJPL} is given in *Parkinson et al. (2015b)* up to altitudes of 112 km, the upper limit of their simulations. Here, we assume that K_{zzJPL} extends with the same exponential slope between 112 and 140 km. The corresponding CO profile $n_{\text{CO, modelJPL}}$ is given in Fig. 6A: it overestimates $n_{\text{CO, SOIR}}$ by a factor up to 3 below 127 km, and underestimates the measured CO densities above these altitudes. Our calculations show that the *von Zahn et al. (1980)*, *Parkinson et al. (2015b)* and *Zhang et al. (2012)* underestimated K_{zz} in the 80–120 km altitude region by substantial factors.

In the case of a non-constant eddy diffusion profile, $K_{\text{zzSOIR, var}}$, the CO homopause is located at ~ 126 km or at a pressure level of 5.8×10^{-5} mbar, where eddy and molecular diffusions are equal.

3.3. Application to the measured He and CO₂ number densities by the Pioneer Venus probe

We revisit the mass spectrometer Pioneer Venus (PV) datasets (*von Zahn et al., 1980*) in order to compute a K_{zz} that extends up to ~ 200 km. We note that *von Zahn et al. (1980)* did not use the actual data measured by the PV probe to determine a $K_{\text{zz, vZ}}(z)$ profile, but rather outputs from a model that best fit the species number density profiles.

Here, we consider the measured He and CO₂ number densities, $n_{\text{CO}_2, \text{PV}}$ and $n_{\text{He, PV}}$, measured between 120 and 200 km (see Table 1 of *von Zahn et al. (1980)*). The PV in-situ data were taken at a latitude of 37.9°S and a longitude of 290.9°W on December 9, 1978 and a local solar time of 8.30 AM. The PV profiles were thus measured 32 years before the SOIR profiles, at a slightly different local solar time (all SOIR measurements are at 6 AM or 6 PM). The 10.7 cm solar flux during the

PV observation was equal to 189.6 standard units, which is slightly larger than during the Venus Express era, which varied between 100 and 150 standard units (*Tapping, 2013*).

For the PV data, the simulations are run considering a CO₂-He atmosphere, neglecting all other species in the simulation, and with a fixed number density for both species at the lower boundary. We compute a temperature profile using Eq. (2) and $n_{\text{CO}_2, \text{PV}}(z)$, see Fig. 7A and Fig. 7B.

We compute K_{zz} profiles that best fit both the SOIR CO and the PV He number density profiles.

Similar to what we did in the previous section, we adjust an altitude-constant K_{zz} profile $K_{\text{zz, cst}}$ and a variable K_{zz} profile $K_{\text{zz, var}}$, variable at four altitude levels, every 10 km between 110 and 140 km, interpolated between those altitude values, and assumed constant above 140 km and below 110 km. The results are presented in Fig. 7C, D, and E.

Even though they are close, the PV and SOIR CO₂ number densities do not overlap in Fig. 7A in the 130–140 km region, as well as the temperature profiles in Fig. 7B. Such differences can be explained by the local solar time difference between the PV and SOIR measurements (6 AM/6 PM for SOIR, 8.30 AM for PV), and by the large atmospheric variability that has been reported in the Venus atmosphere above the cloud deck (*Mahieux et al., 2015a; Piccialli et al., 2015*). Moreover, the SOIR data are mean profiles while the PV data are one single measurement.

In Fig. 7E, we also displayed $K_{\text{zz, vZ}}$ and $K_{\text{zz, JPL}}$. For the latest, we assumed that the K_{zz} profile is constant above 140 km. In Fig. 7C and D, we show the He and CO profiles, respectively, that are obtained considering the respective K_{zz} profile. We observe both for He and CO a disagreement between the modeled profile and the PV and SOIR profiles obtained using the *von Zahn et al. (1980)* and JPL K_{zz} profiles. The agreement is better, but not perfect, when considering the variable K_{zz} profile derived in this work.

We summarize the fitted eddy coefficients, both from the SOIR data only and from the combined SOIR and PV data in Table 1. In this study, we were able to determine an eddy diffusion profile extending from 80

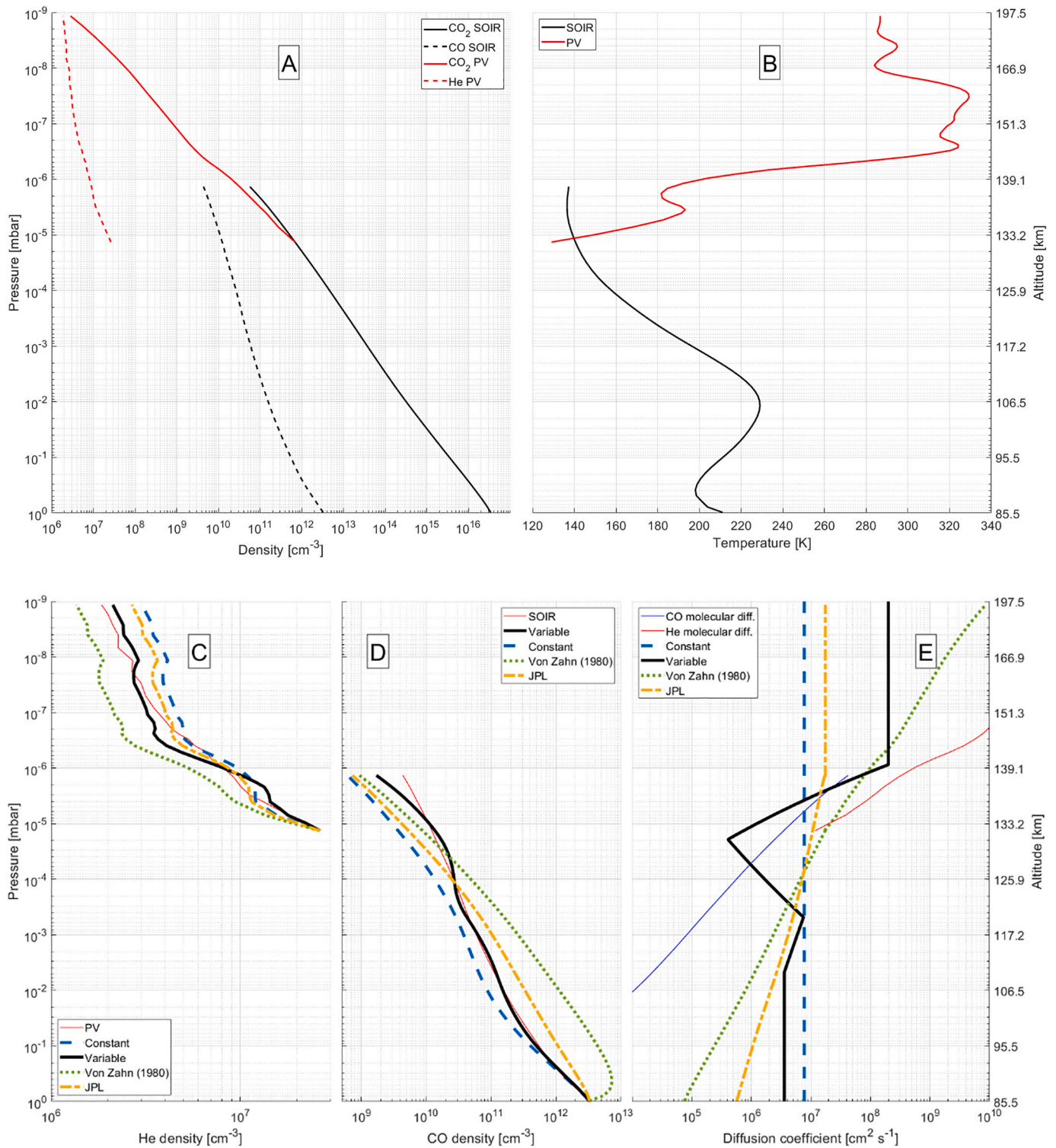


Fig. 7. Panel A: Number density profiles. The CO_2 number density profiles $n_{\text{CO}_2, \text{SOIR}}$ and $n_{\text{CO}_2, \text{PV}}$ are the black and red solid curves, the SOIR CO profile $n_{\text{CO}, \text{SOIR}}$ and the PV He profile $n_{\text{He}, \text{PV}}$ are the black and red dashed curves. Panel B: Temperature profiles, black for SOIR and red for PV. Panel C: Pioneer Venus model profiles. The PV He profile $n_{\text{He}, \text{PV}}$ is the thin red profile (named *PV*). $n_{\text{He}, \text{modelconst}}$ fitted using a constant eddy coefficient profile, is the thick blue dashed profile (named *Constant*) and $n_{\text{He}, \text{modelvar}}$ fitted using a variable eddy coefficient profile, is the thick black plain profile (named *Variable*). $n_{\text{CO}, \text{modelvz}}$, the profile fitted using the [von Zahn et al. \(1980\)](#) profile $K_{zz, \text{vz}}$, is the green thick dotted profile (named *Von Zahn (1980)*), and $n_{\text{CO}, \text{modeljpl}}$, the profiles fitted using the JPL profile, $K_{zz, \text{jpl}}$, is the orange thick dash-dotted profiles (named *JPL*). Panel D: Same as Panel C but for CO from SOIR. Panel E: Molecular diffusion coefficient of CO (thin blue solid) and He (thin red solid). The constant eddy coefficient $K_{zz, \text{cst}}$ is the thick blue dashed curve (named *Constant*), and the variable eddy coefficient profile $K_{zz, \text{var}}$ is the thick black solid curve (named *Variable*). The [von Zahn et al. \(1980\)](#) profile, $K_{zz, \text{vz}}$, is the thick green dotted profile (named *von Zahn et al. (1980)*) and the JPL profile, $K_{zz, \text{jpl}}$, is the thick orange dash-dotted profile (named *JPL*). (For interpretation of the references to colour in this figure legend, the reader is referred to the web version of this article.)

up 200 km of altitude, $K_{zz, var}$, which best fits the SOIR CO and He PV data using the simple 1D-diffusion/photochemical model we presented in this work. This profile is the first attempt, since the work by von Zahn et al. (1980) using the PV data, to evaluate the eddy diffusion coefficient in the Venus mesosphere and thermosphere, and can now be used in Venus photochemical models to model atmospheric diffusion.

4. Conclusion

We present mean CO, CO₂, and temperature profiles derived from the SOIR/Venus Express database.

We compare the mean SOIR number density profiles with steady-state number density profiles from a 1D-photochemical/diffusion model, and adjust the eddy diffusion profile to best fit the model CO number densities with the mean SOIR CO densities. Two vertical eddy diffusion profiles were considered: the first one is constant with altitude, and the second one is variable between 110 km and 130 km.

Using the same approach with the Pioneer Venus Probe He and CO₂ dataset (von Zahn et al., 1980), we compute a hydrostatic temperature profile from the CO₂ number density profile. The eddy diffusion profile that minimizes both the SOIR CO and the Pioneer Venus He profiles is similar to the Earth eddy diffusion profile (Segura et al., 2007), but is different from the von Zahn et al. (1980) results. Our eddy diffusion profile is not perfect, but better than either von Zahn et al. (1980) or Parkinson et al. (2015b). The profile derived in this paper is constant below 110 km ($4.03 \times 10^6 \text{ cm}^2/\text{s}^{-1}$) and above 140 km ($2.41 \times 10^8 \text{ cm}^2/\text{s}^{-1}$), and shows a minimum around 130 km ($4.04 \times 10^5 \text{ cm}^2/\text{s}^{-1}$). Comparisons of the SOIR CO and Pioneer Venus He with computations from our model using the Parkinson et al. (2015b) K_{zz} profile does not show good agreements either.

This is the second attempt to model the eddy diffusion profile from measured density profiles, after von Zahn et al. (1980) using the Pioneer Venus data. The eddy diffusion profile is an important parameter for modelling atmospheres, and the values reported in this work can be used in Venus photochemical models: they were derived by fitting observations using a simple 1D photochemical/diffusion model combining SOIR and Pioneer Venus data.

Declaration of Competing Interest

None.

Acknowledgments

Venus Express is a planetary mission from the European Space Agency (ESA). We wish to thank all ESA members who participated in the mission, in particular, H. Svedhem and D. Titov. We thank our collaborators at IASB-BIRA (Belgium), Latmos (France), and IKI (Russia). The research program was supported by the Belgian Federal Science Policy Office and the European Space Agency (ESA, PRODEX program, contracts C 90268, 90113, 17645, 90323, and 4000107727). A. Mahieux was supported by the Marie Skłodowska-Curie Action from the European Commission under grant number 838587. S. Robert thanks BELSPO for the FED-tWIN funding (Prf-2019-077 - RT-MOLEXO). F. Mills was supported by NASA grant NNX16AN03G to SSI.

References

Banks, P.M., Kockarts, G., 1973. *Aeronomy Part B*. Academic Press, New York.
 Chamberlain, S., et al., 2020. SOIR/VEX observations of water vapor at the terminator in the Venus mesosphere. *Icarus*. 346, 113819.
 Chan, W., Cooper, G., Brion, C., 1993. The electronic spectrum of carbon dioxide. Discrete and continuum photoabsorption oscillator strengths (6-203 eV). *Chem. Phys.* 178, 401–413.
 Edmon Jr., H., Hoskins, B., McIntyre, M., 1980. Eliassen-palm cross sections for the troposphere. *J. Atmos. Sci.* 37, 2600–2616.
 Fox, J.L., Bougher, S.W., 1991. Structure, luminosity, and dynamics of the Venus thermosphere. *Space Sci. Rev.* 55, 357–489.

Hedin, A.E., Niemann, H.B., Kasprzak, W.T., 1983. Global empirical model of the Venus thermosphere. *J. Geophys. Res.* 88, 73–83.
 Huestis, D.L., Berkowitz, J., 2010. Critical evaluation of the photoabsorption cross section of CO₂ from 0.125 to 201.6 nm at room temperature. In: Bhardwaj, A. (Ed.), *Planetary Science*. World Scientific Publishing Company.
 Inn, E.C.Y., Heimerl, J.M., 1971. The photolysis of CO₂ at wavelengths exceeding 1740 Å. *J. Atmos. Sci.* 28, 838–841.
 Ityakov, D., Linnartz, H., Ubachs, W., 2008. Deep-UV absorption and Rayleigh scattering of carbon dioxide. *Chem. Phys. Lett.* 462, 31–34.
 Krasnopolsky, V.A., 2012. A photochemical model for the Venus atmosphere at 47–112 km. *Icarus*. 218, 230–246.
 Krasnopolsky, V., Parshev, V.A., 1983. Photochemistry of the Venus atmosphere. In: Hunten, D.M., Colin, L., Donahue, T.M., Moroz, L.V. (Eds.), *Venus*. University of Arizona Press, Tucson, pp. 431–458.
 Lane, W.A., Opstbaum, R., 1983. High altitude Venus haze from Pioneer Venus limb scans. *Icarus*. 54, 48–58.
 Lawrence, G., 1972. Production of O(1S) from photodissociation of CO₂. *J. Chem. Phys.* 57, 5616–5617.
 Mahieux, A., et al., 2008. In-flight performance and calibration of SPICAV/SOIR on-board Venus express. *Appl. Opt.* 47, 2252–2265.
 Mahieux, A., et al., 2012. Densities and temperatures in the Venus mesosphere and lower thermosphere retrieved from SOIR on board Venus express: carbon dioxide measurements at the Venus terminator. *J. Geophys. Res.* 117, E07001.
 Mahieux, A., et al., 2015a. Update of the Venus density and temperature profiles at high altitude measured by SOIR on board Venus express. *Planet. Space Sci.* 113–114, 309–320.
 Mahieux, A., et al., 2015b. Venus mesospheric sulfur dioxide measurement retrieved from SOIR on board Venus express. *Planet. Space Sci.* 113–114, 193–204.
 Mahieux, A., Wilquet, V., Vandaele, A.C., Robert, S., Drummond, R., Bertaux, J.L., 2015c. Hydrogen halides measurements in the Venus upper atmosphere retrieved from SOIR on board Venus express. *Planet. Space Sci.* 113–114, 264–274.
 Marrero, T., Mason, E., 1972. Gaseous diffusion coefficients. *J. Phys. Chem. Ref. Data* 1, 3–118.
 Mills, F.P., Allen, M., 2007. A review of selected issues concerning the chemistry in Venus' middle atmosphere. *Planet. Space Sci.* 55, 1729–1740.
 Nevejans, D., et al., 2006. Compact high-resolution space-borne echelle grating spectrometer with AOTF based on order sorting for the infrared domain from 2.2 to 4.3 micrometer. *Appl. Opt.* 45, 5191–5206.
 Okabe, H., 1978. *Photochemistry of Small Molecules*. New York.
 Parkinson, W.H., Rufus, J., Yoshino, K., 2003. Absolute absorption cross section measurements of CO₂ in the wavelength region 163–200 nm and the temperature dependence. *Chem. Phys.* 290, 251–256.
 Parkinson, C., Gao, P., Esposito, L., Yung, Y., Bougher, S.W., Hirtzig, M., 2015a. Photochemical control of the distribution of Venusian water. *Planet. Space Sci.* 113–114, 226–236.
 Parkinson, C., et al., 2015b. Distribution of Sulphuric acid aerosols in the clouds and upper haze of Venus using Venus express VAST and VeRa temperature profiles. *Planet. Space Sci.* 113–114, 205–218.
 Piccialli, A., et al., 2015. Thermal structure of Venus upper atmosphere measured by stellar occultations with SPICAV/Venus express. *Planet. Space Sci.* 113–114, 321–335.
 Segura, A., Meadows, V.S., Kasting, J.F., Crisp, D., Cohen, M., 2007. Abiotic formation of O₂ and O₃ in high-CO₂ terrestrial atmospheres. *A&A*. 472, 665–679.
 Stark, G., Yoshino, K., Smith, P.L., Ito, K., 2007. Photoabsorption cross section measurements of CO₂ between 106.1 and 118.7 nm at 295 and 195K. *J. Quant. Spectrosc. Radiat. Transf.* 103, 67–73.
 Tapping, K.F., 2013. The 10.7 cm solar radio flux (F10.7). *Space Weather*. 11, 394–406.
 Trompet, L., et al., 2017. Description, accessibility and usage of SOIR/Venus express atmospheric profiles of Venus distributed in VESPA (virtual European solar and planetary access). *Planet. Space Sci.* 150, 60–64.
 Vandaele, A.C., Mahieux, A., Robert, S., Drummond, R., Wilquet, V., Bertaux, J.L., 2015. Carbon monoxide short term variability observed on Venus with SOIR/VEX. *Planet. Space Sci.* 113–114, 237–255.
 Vandaele, A.C., et al., 2016a. Contribution from SOIR/VEX to the updated Venus International reference atmosphere (VIRA). *Adv. Space Res.* 57, 443–458.
 Vandaele, A.C., et al., 2016b. Carbon monoxide observed in Venus' atmosphere with SOIR/VEX. *Icarus*. 272, 48–59.
 von Zahn, U., Fricke, K.H., Hunten, D.M., Krankowsky, D., Mauersberger, K., Nier, A.O., 1980. The upper atmosphere of Venus during morning conditions. *J. Geophys. Res.* 85, 7829–7840.
 Woo, R., Armstrong, J.W., Ishimaru, A., 1980. Radio occultation measurements of turbulence in the Venus atmosphere by Pioneer Venus. *J. Geophys. Res. Space Physics* 85, 8031–8038.
 Woods, T.N., et al., 2005. The solar EUV experiment (SEE): Mission overview and first results. *J. Geophys. Res.* 110.
 Yelle, R., Mahieux, A., Morrison, S., Vuitton, V., Hörst, S., 2014. Perturbation of the Mars atmosphere by the near-collision with comet C/2013 A1 (siding spring). *Icarus*. 237, 202–210.
 Yoshino, K., Esmond, J.R., Parkinson, W.H., Ito, K., Matsui, T., 1996. Absorption cross section measurements of water vapor in the wavelength region 120 to 188 nm. *Chem. Phys.* 211, 387–391.

Yung, Y.L., DeMore, W.B., 1982. Photochemistry of the stratosphere of Venus: implications for atmospheric evolution. *Icarus*. 51, 199–247.

Zasova, L.V., Moroz, V.I., Linkin, V.M., Khatountsev, I.A., Maiorov, B.S., 2006. Structure of the Venusian atmosphere from surface up to 100 km. *Cosm. Res.* 44, 364–383.

Zhang, X., Liang, M., Mills, F., Belyaev, D., Yung, Y., 2012. Sulfur chemistry in the middle atmosphere of Venus. *Icarus*. 217, 714–739.